Nanoscale

PAPER

Check for updates

Role of the microridges on cactus spines

Lin Guo, [a] Satish Kumar, [b] Mingyang Yang, [c] Guihua Tang [*c] and Zhigang Liu[*a]

Cactus spines have inspired a wide range of micro- and nano-structures that cause droplets to move spontaneously and directionally. The conical shape and the surface wettability gradient are two typical characteristics in such systems. The cross section of the existing conical fibers is usually assumed to be an ideal circle. In fact, microridges are observed on the spine surface of the cactus, and the function is not yet fully understood. The present work thus focuses on how microridges affect droplet self-transport. Structures mimicking microridges are first investigated by constructing pyramidal cross sections with concave or convex lateral faces. The dissipative particle dynamics method is then employed to numerically investigate and theoretically analyze the dynamic behaviors of droplets on these conical fibers with different cross sections. The results show that the microridges reduce the base radius and the contact area of the droplet, thereby increasing the driving force and reducing the friction force. Moreover, by mimicking the microridges structure, we propose a conical fiber with a triple concave cross section, which increases the droplet velocity and the distance traveled over the traditional circular fiber. This work reveals the role of the microridges in the droplet self-transport, which opens up new prospects for the manufacture of fiber systems for microfluidics and liquid manipulation.

1. Introduction

Natural biological organisms often use self-propelled directional liquid transport (SDLT)[1,2] as a smart strategy to exploit ambient water vapor. By not requiring extra energy, SDLT has attracted significant interest for a wide range of applications, including fog harvesting,[3,4] liquid pumping,[5,6] liquid diodes,[7] microfluidic devices,[8] oil–water separation,[9] bubble collection,[10] condensers[11] and so forth. A variety of natural structures such as shorebird beak,[12] spider silk,[13] cactus spine,[14,15] and Nepenthes Alaska[16,17] provide rich inspirations for directional liquid transportation. To date, the structural gradient inspired by cactus spines has typically been used as the main driving force to collect water driven by the Laplace pressure difference.

Numerous structures mimicking cactus spines have been developed and exhibit extraordinary droplet manipulation capabilities, which can be classified into five categories according to their shapes: single conical spine,[18–29] conical spine clusters,[30] two-dimensional triangles,[31] superhydrophilic wedges on superhydrophobic surfaces,[32–35] and conical grooves.[36–38] For instance, Wang et al.[19] fabricated a spine with barbs and hierarchical channels that cause water to move spontaneously, greatly improving fog harvesting. Li et al.[30] replicated real natural clusters of branched spines and reported a cactus-inspired surface decorated with multiple directional artificial spines. Bai et al.[31] simplified cactus spins from a three-dimensional cone to a two-dimensional triangle and designed a cactus kirigami for efficient water harvesting. Chen et al.[32] fabricated a wedge superhydrophilic chip capable of spontaneous and directional droplet transportation. Huang et al.[36] reported an anisotropic surface with radially arranged omniphobic microstripes, on which droplets can self-transport with lossless liquid residue.

To design the structure and prepare superior functional surfaces based on cactus spines, one must first understand the mechanism behind the self-propelled droplet transport on a conical fiber. Lv et al.[25] experimentally studied water droplet motion on tapered surfaces and concluded that the total free energy and driving force exerted on a droplet are determined by the substrate curvature and substrate curvature gradient. Gurera et al.[22] systematically studied the effect of conical geometry by considering the tip angle, cone length, surface area, and inclination angle. The present authors also experimentally studied the directional motion of a single droplet on cactus spines and revealed that the Gibbs free energy transforms into kinetic energy to overcome the friction loss caused by fluid viscosity.[15]

[a] Energy Research Institute, Qilu University of Technology, Jinan 250014, P.R. China.
E-mail: zgliu9322@163.com
[b] G. W. Woodruff School of Mechanical Engineering, Georgia Institute of Technology, Atlanta, GA 30332, USA
[c] MOE Key Laboratory of Thermo-Fluid Science and Engineering, School of Energy and Power Engineering, Xi'an Jiaotong University, Xi'an 710049, P. R. China.
E-mail: ghtang@mail.xjtu.edu.cn

Much of the above work involves the design and fabrication of conical cones with ideal circular cross sections. With the in-depth understanding of the structure, the microridges are observed on cactus spines.[15] The cross section of the spine is actually uneven, as opposed to a perfectly smooth circle. Inspired by this, Hu *et al.*[1] developed conical fibers with a pyramidal-structured cross section which enables ultrafast droplet transportation. It has been shown that the cross section of conical fibers is crucial for determining the droplet transport. However, the function of micro-ridges has heretofore been poorly understood, so the present work focuses on the role of microridges in droplet self-transport. The results reveal the potential of the new structure to drive droplets. Note that the droplets self-propulsion has been realized *via* gradient surface chemistry[39] and chemical patterns.[40] Zhang *et al.*[40] fabricated a gradient quasi-liquid surface to drive droplets with surface tension down to 10.0 mN m^{-1}. Still, chemical coatings may face problems of unsuitable application scenarios and durability. In this case, structural driving can be an effective alternative. Moreover, the combination of the structure design and chemical coatings is expected to realize more complex functionalities.

Molecular dynamics simulations have drawn attention as a way to address mesoscale problems in complex fluids and soft matter.[41–45] The present work applies the classical computational algorithm of dissipative particle dynamics (DPD) to take advantage of the large timescales in lattice-gas automata and mesh-free algorithms in molecular dynamics.[46] Therefore, to explore the role of microridges on cactus spines, a numerical study of the cross-sectional structure effect on droplet self-motion is conducted in the present work. To mimic the uneven cross-sectional structure, the pyramid shapes with concave or convex individual sides are designed. Five types of cross sections are simulated to investigate the droplet dynamics. The moving velocity and the maximum moving distance of nanodroplets along conical fibers are analyzed. The effects of surface wettability, cone angle, surface tension, and droplet size on droplet self-motion are also explored. The present study improves our understanding of self-driven transport and thereby supports efforts to design efficient conical fibers.

2. Numerical methodology

2.1. Mimetic structures of microridges

We experimentally studied the SDLT on spines of Mammillaria elongata var. intertexta cactus,[15] an example of which is shown in Fig. 1(a). The droplet moves spontaneously from the tip to the base of the spine due to the Laplace pressure difference. Fig. 1(b) exhibits the microstructure of a cactus spine captured by field emission scanning electron microscope (Hitachi-SU8010, Japan). Microridges are observed on the conical surface of the spine, as shown in Fig. 1(c). To explore the role of microridges in SDLT, conical fibers with cross sections of pyramidal geometry are constructed. Two types of side faces (concave and convex) and two side numbers (three and five) are designed, and are labeled tri-concave, penta-concave, tri-convex, and penta-convex, respectively. Note that the studied five geometries share the same radius of the circular base, which is shown as the dashed circle in Fig. 1(d). The fiber length L is fixed at 80, and the conical half-angle α is 7.1°.

## 2.2. Basic settings for modeling with dissipative particle dynamics

The dissipative particle dynamics (DPD) method is carried out using the Large-scale Atomic/Molecular Massively Parallel Simulator (LAMMPS). The basic component of DPD is a lump of molecules, which represents molecular clusters rather than atoms or molecules themselves.[47] The hybrid mdpd/rhosum and mdpd pair styles are applied to describe the interactions between fluid particles and solid particles. The mdpd/rhosum style computes the local particle mass density ρ for mDPD particles by kernel function interpolation. Interactions between mDPD particles are given by[44]

$$\mathbf{F}_{ij}^{C} = Aw_{c}(r_{ij})\mathbf{e}_{ij} + B(\rho_i + \rho_j)w_{d}(r_{ij})\mathbf{e}_{ij}, \tag{1}$$

$$\mathbf{F}_{ij}^{D} = -\gamma w_{D}(r_{ij})(\mathbf{e}_{ij} \cdot \mathbf{v}_{ij})\mathbf{e}_{ij}, \tag{2}$$

$$\mathbf{F}_{ij}^{R} = \sigma w_{R}(r_{ij})\xi_{ij}\Delta t^{-1/2}\mathbf{e}_{ij}, \tag{3}$$

where $\mathbf{F}_{ij}^{C}$, $\mathbf{F}_{ij}^{D}$, and $\mathbf{F}_{ij}^{R}$ represent the conservative, dissipative, and random forces, respectively. The computational parameters used in the present simulations are detailed in Table 1.
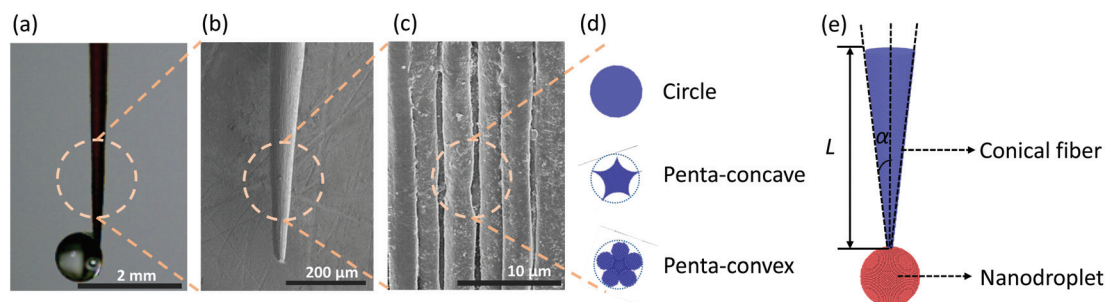
Fig. 1 (a) The self-transport of a droplet on a cactus spine. (b) Microstructures of the conical spine. (c) Microridges observed on the spine surface. (d) Pyramid cross-sections mimicking the microridges. Two types of cross-section structures (concave and convex) are considered with different side numbers. Penta-concave and penta-convex with five sides are shown as examples. (e) Initial computational setup of a nanodroplet placed on a conical fiber with different cross-sections. L represents the total fiber length. α represents the conical half-angle.

Table 1 Potential parameters: all quantities are given in DPD units, and subscripts l and s stand for liquid particles and solid particles, respectively

Parameters	Symbol	Value
Attraction parameter	A_{ll}, A_{ss}	−40.00
Repulsion parameter	B_{ll}, B_{ss}, B_{sl}	25.00
Dissipation parameter	γ	18.00
Cut off radius of attractive force	r_c	1.00
Cut off radius of repulsive force	r_d	0.75
Particle density	ρ	6.00

By using DPD method, all the results are given in model specific, *i.e.*, DPD units, and used for calculation.[44,48]

Simulations are performed in a mutually perpendicular computational region of size 80 × 80 × 200. First, to explore the SDLT process, a liquid drop is placed on a conical fiber mimicking the experimental process, as shown in Fig. 1(e). The coordinates of the fiber tip are (0, 0, 0), and the droplet is under the fiber tip. The periodic boundary conditions are assigned in the three mutually perpendicular directions. A modified velocity-Verlet algorithm is used for the numerical integration of the many-body DPD equations.[49] To realize the self-propelled motion, the droplet is placed on the solid surface and then equilibrated for 50 000 steps with a timestep of 0.01. The droplet-conical fiber system minimizes its surface energy, which leads to the droplet movement.

3. Results and discussion

3.1. Validation of computational method

To validate the proposed algorithm, the SDLT of droplets on conical fibers with different initial droplet positions is explored. Two cases are considered: the droplet initially placed on the tip and on the base of a conical fiber. Taking the conical fiber with circular cross section as an example, Fig. 2 shows the droplet motion as a function of time. The attraction number A_{sl} is set to 18, and the droplet radius R is 6. The results show that once the droplet is placed on the fiber tip, it moves spontaneously from tip to base (see Fig. 2(a)). When placed at the fiber base, the droplet remains immobile (see Fig. 2(b)). The spontaneous and directional movement of the droplet is consistent with the reported experimental obervations,[15] which validates the present computational method.

## 3.2. Structure suitable for imitating microridges

To find out the structure suitable for imitating microridges on spine surfaces, the dynamic behaviors of droplets on four types of cross sections (tri-concave, penta-concave, tri-convex, and penta-convex) are investigated. Time-lapsed images during the movements are plotted in Fig. 3, where droplet radius $R =$ 6 and conical angle $\alpha = 7.1°$.

First, note that all the four types of conical fibers exhibit a capability in SDLT. As shown in Fig. 3, all the droplets spontaneously move from tip to base. However, the droplet dynamics differ. To quantitatively describe the droplet dynamics, we calculate the average moving velocity v_{ave} and the maximum moving distance z_{max} traveled for different cross sections and droplet sizes, as shown in Fig. 3(e). Here the average droplet velocity v_{ave} covers the time span from the moment that the droplet begins to move along the fiber, *i.e.*, the centroid z-coordinates of the droplet equals 0, to the moment that the droplet reaches z_{max}.
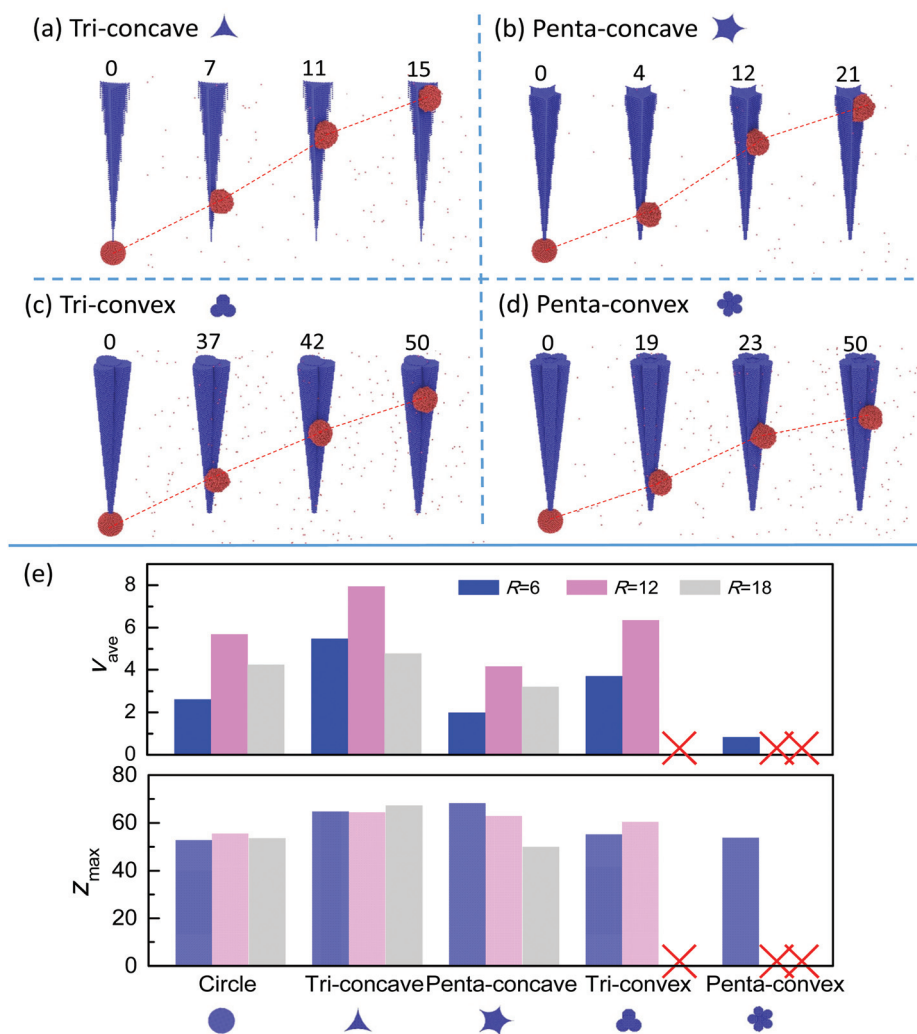
The results show that the tri-convex case fails to drive the droplet for a droplet radius greater than 18 and the penta-convex case fails when a droplet radius is greater than 12. This restriction of droplet size means that the pyramidal cross section with convex side surfaces is not suitable for studying the function of microridges. In contrast, all the droplets spontaneously move when the side surfaces are concave. In addition, compared with the circular case, the tri-concave case produces a greater velocity and traveling distance, indicating a significant potential for driving droplets. However, the droplets move more slowly on the penta-concave fiber than on the circular fiber. The maximum distance z_{max} is essentially independent of droplet size between the circle and tri-concave cases but decreases with the increasing droplet size for the penta-concave case. Overall, the concave structure is the most suitable structure for mimicking microridges on cactus spines.

3.3. Two modes of motion

Prior to discussing the role of microridges, the modes of droplets motion during SDLT should be clarified first. Two modes of motion are summarized as a function of droplet size, as
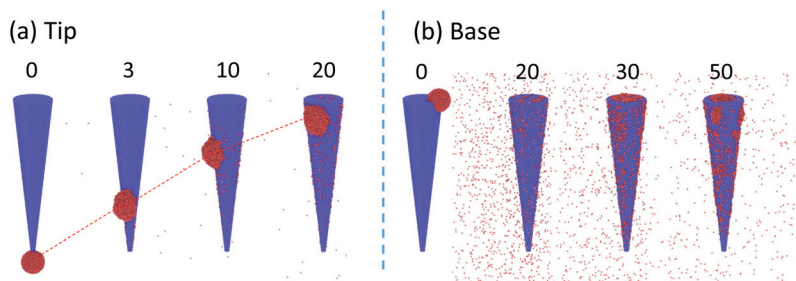
Fig. 2 Validation of droplet self-driven motion on the conical fiber. Droplet is initially placed at (a) the tip and (b) the base of a conical fiber. Cases with droplet radius R = 6 and conical angle α = 7.1° are shown as examples.

Fig. 3 Time-lapsed images of droplet self-driven process on cross sections of (a) tri-concave, (b) penta-concave, (c) tri-convex, and (d) penta-convex. Cases with droplet radius $R = 6$ and conical angle $\alpha = 7.1°$ are shown as examples. (e) Droplet average velocity v_{ave} and the maximum distance z_{max} under various cross sections and droplet sizes. Timesteps are marked above spines in DPD units.
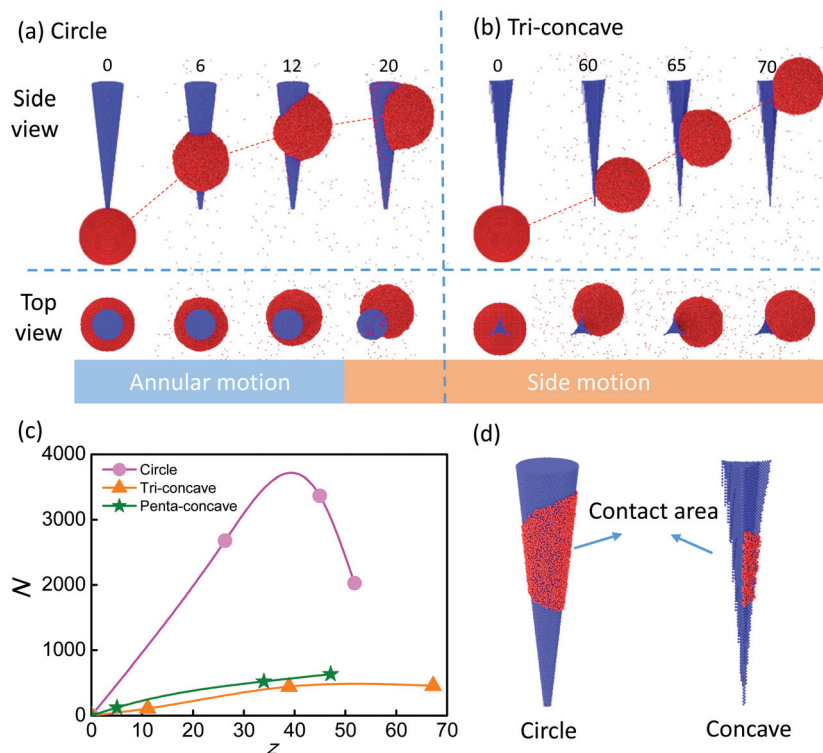
shown in Fig. 4(a) and (b). Droplets moving on the circle and tri-concave cross sections are given as examples with droplet radius $R = 18$ and conical angle $\alpha = 7.1°$. In Fig. 4(a), when the fiber radius is relatively small compared with the droplet size, the droplet moves annularly on the circular fiber, which is referred to herein as "annular motion". Given the continuous movement of the droplet and the increasing radius of the fiber, the droplet cannot wrap around the fiber, so it moves along the side of the fiber. The mode of motion thus changes from annular motion to "side motion". For the pyramidal cross section, the droplet always moves laterally on the fiber, regardless of the fiber radius and droplet size, as shown in Fig. 4(b).

Fig. 4(c) gives the contact numbers of the liquid and solid particles for the circular, tri-concave, and penta-concave cases. The contact number for the circular fiber first increases and then decreases as the mode of motion changes from annular motion to side motion. The side motion produces a smaller

contact area than the annular motion. Fluid particles are easier to contact with each other on the circular conical fiber with continuous convex surface, as shown in Fig. 4(d), in which particles in contact are in red. For the fiber with pyramidal cross sections with concave sides, fluid particles are gathered by the surface tension and separated by edges, resulting in side motion. From the above discussion, it can be inferred that microridges can make the contact area longer and narrower, leading to a smaller contact area. The process of droplet movement could thus produce less fluid residue, and the resistance to motion could also decrease because of the reduced contact area.

3.4. Theoretical model

This section presents a theoretical model to reveal the mechanism of droplet self-motion on concave cross sections. Conical fibers with concave cross section illustrate a different self-transport mode of motion than the circular case. The results

Fig. 4 Two modes of droplets motion on conical fibers: annular motion (a) and side motion (b). Droplets moving on circular and tri-concave cross section are shown as examples with droplet radius $R = 18$ and conical angle $\alpha = 7.1°$. (c) Numbers of contact particles N along the z-coordinate under different cross sections. (d) Examples of contact areas on fibers with circular and concave cross sections. Contacted fluid particles are marked in red.

in Fig. 3(e) show that the concave side number also seems to affect SDLT. Droplets have larger velocities on the tri-concave compared with on the circular, but with smaller velocities for the penta-concave. Therefore, the effects of both the concave structure and the side number are considered. It should be noted that the droplet size is on the same scale with the fiber considering the feasibility of the simulation. Therefore, the droplet only moves on one side surface in the present simulation, and the theoretical model is established on the assumption that the droplet moves in the side motion.

Generally, the self-driven motion of a droplet on a conical fiber is driven by the Laplace pressure difference. For a droplet on a circular conical fiber, as schematic in Fig. 5(a), the Laplace pressure difference Δp is given by

$$\Delta p = 2\gamma \left(\frac{1}{r_1} - \frac{1}{r_2} \right) = 2\gamma L \left(\frac{1}{z_1} - \frac{1}{z_1 + l_z} \right) \frac{1}{r_b}, \quad (4)$$

where γ is the surface tension, r is the radius of the fiber, subscripts 1 and 2 refer to the two sides of the droplet, l_z is the droplet length in the z direction, and r_b is the base fiber radius.

We assume that, for fibers with pyramidal cross section and concave sides, the Laplace pressure difference arises from two sources. One source is the entire conical shape of the fiber, which contributes a Laplace pressure difference Δp_{equal}. The second source is the individual concave sides that compose the entire conical fiber and contribute a Laplace pressure difference $\Delta p_{concave}$. The cross sections of tri-concave and penta-concave fibers are shown in Fig. 5(b) and (c), respectively. To calculate Δp_{equal}, the pyramidal cross section is transferred to an equivalent circle with radius r_{equal}. The half side length of the polygon circumscribed about the base circle $r_{polygon}$ is

$$r_{polygon,i} = \tan \frac{\pi}{i} \cdot r_b, \quad (5)$$

where i refers to the concave side number. The surface area of the equivalent circle, based on the equivalent radius, is

$$r_{equal,i} = \sqrt{\frac{S_{equal,i}}{\pi}} = \sqrt{\frac{i}{\pi} \tan \frac{2\pi}{i} - \left(\frac{i}{2} - 1 \right) \tan 2 \left(\frac{\pi}{i} \right)} \cdot r_b. \quad (6)$$

Thus, the Laplace pressure differences caused by the entire conical fiber and the individual concave surfaces can be respectively quantified as

$$\Delta p_{equal,i} = 2\gamma \left(\frac{1}{r_{equal,i}} - \frac{1}{r_{2,equal,i}} \right) = 2\gamma L \left(\frac{1}{z_1} - \frac{1}{z_1 + l_z} \right) \cdot \frac{1}{r_{equal,i}}, \quad (7)$$

$$\Delta p_{concave,i} = 2\gamma \left(\frac{1}{r_{2,polygon,i}} - \frac{1}{r_{1,polygon,i}} \right). \quad (8)$$
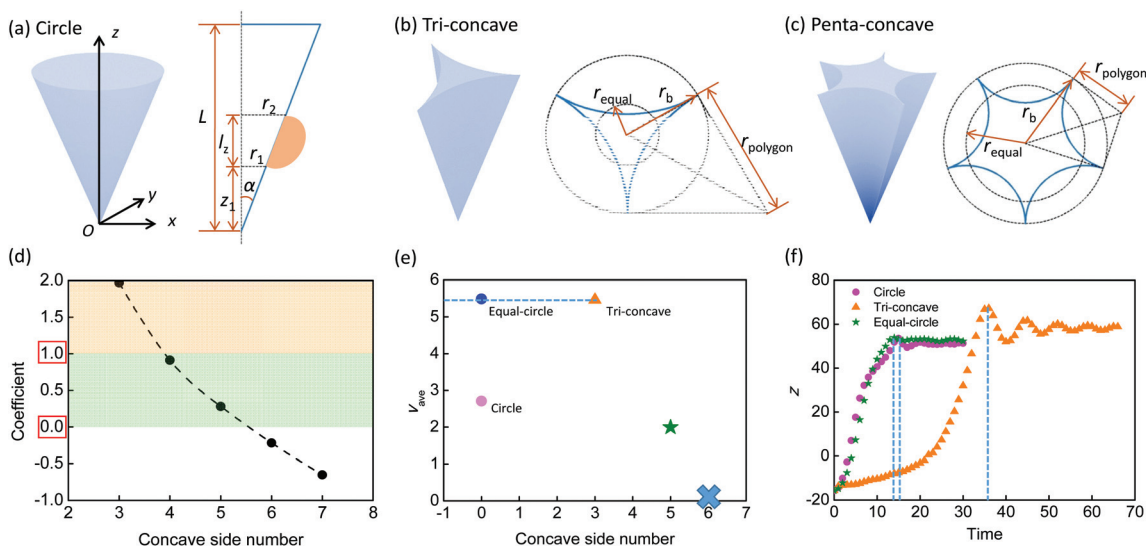
Fig. 5 Schematic diagram of conical fibers with (a) circular, (b) tri-concave and (c) penta-concave cross sections. Cross section images of xz plane and xy plane are drawn for theoretical analysis. (d) Coefficient c under different numbers of concave faces. Droplets move faster on concave cross-sections than on circular cross-section if $c > 1$, but slower if $0 < c < 1$. When $c < 0$, the droplet cannot move. (e) Average velocity v_{ave} under different concave faces. The conical fiber with circular cross section is plotted for comparison, whose radius is the equal radius of the tri-concave case. (f) Droplet moving distance in the z direction against time for conical angle $\alpha = 7.1°$ and droplet radius $R = 18$.

The total driving force for a droplet undergoing side motion on a pyramidal structure with concave sides in the $+z$ direction is

$$\Delta p_i = \Delta p_{equal,i} + \Delta p_{concave,i} = c_i \cdot \Delta p, \quad (9)$$

where the coefficient c is the driving force multiple of the concave cases and the circular case. Eqn (9) gives the relationship between the total driving force and the side number, as shown in Fig. 5(d). The results indicate that the coefficient decreases with an increasing number of concave faces. Droplets move faster over the concave cross sections than over the circular cross section if $c > 1$ (yellow zone), but slower if $0 < c < 1$ (green zone). When $c < 0$ (white zone), the droplet cannot move. As the number of concave side increases, the Laplace pressure difference in the $-z$ direction increases accordingly, which minifies the total driving force. The coefficient is negative when the number increases to six, so the droplet cannot move.

To verify the proposed model, the following three factors are presented. First, as shown in Fig. 5(e), when the concave side number increases, the droplet velocity decreases and approaches zero if $i = 6$, which is consistent with the trend shown in Fig. 5(d). Second, the equivalent conical fiber for the tri-concave case ($r_b = r_{equal,3}$) is constructed, and the droplet velocity is marked as equal-circle in Fig. 5(e). The droplet on the equal-circle undergoes annular motion, resulting in a larger contact area and thus a larger friction force than on the tri-concave. However, the driving force of the tri-concave case is smaller than that of the equal-circle case due to the shape of the concave sides. As a result, the droplet velocity for these two cases is almost identical.

The droplet moving distance in the z direction for these two cases can also be used to verify the proposed theoretical model, as shown in Fig. 5(f). For a circular conical fiber, there is only one type of the Laplace pressure difference, which is caused by the convex surface. Droplets move smoothly from the fiber tip to the maximum distance and then keeps steady at around 15 (circle case) and 13 (equal-circle case). In contrast, for the tri-concave case, the droplet initially moves smoothly to the maximum distance, but starts to oscillate back and forth after time = 35. The reason is that $\Delta p_{concave}$ gets larger but Δp_{equal} gets smaller as z_1 increases based on eqn (4). When the droplet reaches z_{max}, $\Delta p_{concave}$ is relatively large and makes the droplet move in the $-z$ direction. The transverse motion of droplets confirms the existence of $\Delta p_{concave}$. Therefore, we conclude that the microridges on cactus spines can reduce the base radius and contact area, thereby increasing the driving force and reducing the frictional force during SDLT.

Note that the above analysis assumes that the droplet length l_z remains the same for these three cases. However, based on the experimental results of Hu et al.,[1] the droplet is stretched by concave surfaces and the droplet length in the z direction of the tri-concave surface exceeds that of the circular case. The driving force of tri-concave case is further enlarged by the extended l_z. Eqn (4) shows that a larger droplet size corresponds to a longer l_z, and therefore a higher driving force. However, the frictional resistance increases with contact area, so the velocity increases first and then decreases, as shown in Fig. 3(e).

3.5. Influencing factors

The investigation of microridges function shows that conical fibers with tri-concave cross sections demonstrate significant potential for driving droplets. Compared with the original

conical fibers with circular cross section, the tri-concave cross section leads to a larger velocity and a greater moving distance. Eqn (9) can be used to show that, given the same basic fiber radius r_b, the driving force for a tri-concave fiber is always greater than that of a fiber with circular cross section. The tri-concave fiber produces the largest driving force, and the droplets always undergo side motion. Based on this structure, the effects of conical angle, liquid surface tension, and surface wettability on SDLT are discussed in this section.

3.5.1. Conical angle of fiber. Three types of tri-concave fibers with conical angles of 7.1°, 14°, and 20.6° are built. Circular-cross-section fibers with different conical angles are also simulated for comparison. The average velocity v_{ave} and the maximum moving distance z_{max} under different conical angles α are shown in Fig. 6(a) and (b), respectively. The results show that all the droplets move spontaneously despite the increase in conical angle. For circular fibers, the droplet moves slower as the conical angle increases, but the moving distance does not decrease much. Droplets move faster on the tri-concave fiber than on the circular fiber and this promotion gets larger as the conical angle increases. However, the moving distance is greatly reduced for the tri-concave case. With the increase of the conical angle, the base fiber radius becomes

larger. Thus, based on eqn (4), the Laplace pressure difference gets smaller, resulting in a velocity reduction. Benefitting from the tri-concave shape, the equivalent base radius increases slightly, leading to a slight reduction of the total driving force and thus a small reduction of the velocity. Overall, a small conical angle is preferable for SDLT on conical fibers.

3.5.2. Surface tension of droplet. The surface tension of the liquid is firstly calculated and the simulation setting up is shown in Fig. 6(c). The simulation is performed in a computational zone of $30 \times 10 \times 10$ with periodic boundary conditions assigned in all directions. Six thousand liquid particles are placed in a zone of $10 \times 10 \times 10$. The system is equilibrated for 100 000 steps with a timestep of 0.01, and the pressure is then averaged for another 100 000 steps. The surface tension is calculated as

$$\gamma = \frac{L}{2}\left[p_{xx} - \frac{1}{2}(p_{yy} + p_{zz})\right], \tag{10}$$

where L is the box length in the x-direction, and p_{xx}, p_{yy}, and p_{zz} are the pressure components. The surface tension can be tuned *via* the attraction parameter A_{ll}, as shown in Fig. 6(c). Fig. 6(d) gives the average velocity under various surface ten-
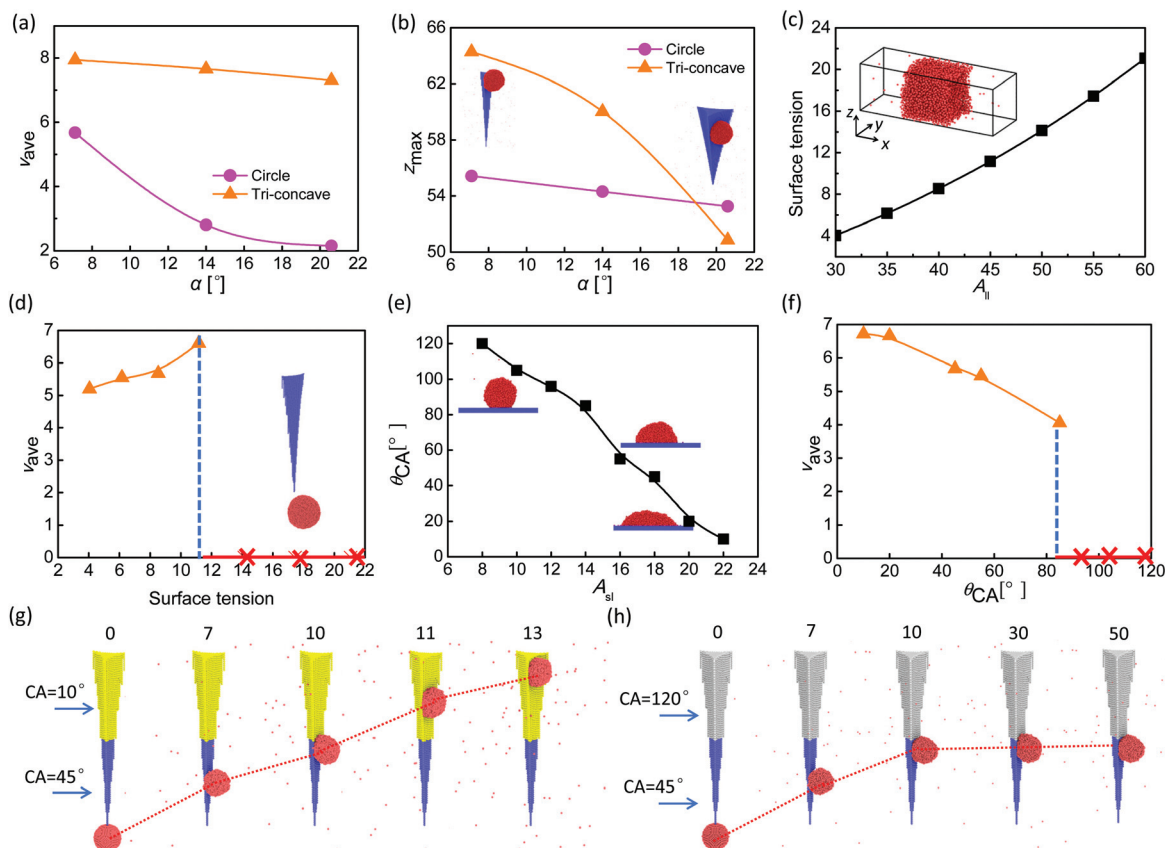
Fig. 6 Influencing factors. The average velocity v_{ave} and maximum moving distance z_{max} under different conical angles α are plotted as (a) and (b), respectively. The insets are for tri-concave with α of 7.1° and 20.6°. (c) Surface tension of the liquid adjusted by attraction parameter A_{ll}. (d) Average moving velocity against surface tension. Droplet detachments are found if the surface tension is too large. (e) Surface wettability against energy parameter A. (f) Average velocity under different surface contact angles. Time-lapsed images on (g) dual-HPI (grafted with contact angle 10°) and (h) dual-HPO cases (grafted with contact angle 120°). The droplet size R = 12.

sions. When the surface tension exceeds 11.17, the droplets cannot wet the solid surface and are detached from the fiber, so no SDLT is observed in these cases, shown as crosses in Fig. 6(d). As the surface tension decreases, the droplet wets and moves along the conical fiber. Despite the velocity reduction, droplets with small surface tension can still move spontaneously. We believe that this result benefits from the individual concave side surfaces. Liquid particles with low surface tension easily spread over the solid surfaces. However, the concave shape of the lateral surface can prevent the spreading and gather the liquid particles together, see Fig. 4(d). As a result, the droplets form and then move in side motion. The tri-concave fiber shows great potential in driving droplets with low surface tension.

3.5.3. Surface wettability. To study the wettability, the surface wetting states ranging from hydrophobic (HPO) to hydrophilic (HPI) are achieved by adjusting the conservative solid–liquid interactions A_{sl}. The contact angles under different A_{sl} are plotted in Fig. 6(a). The performance of droplets on surface with different wettability can be obtained, as shown in Fig. 6(b). The droplet moves more slowly as the contact angle increases. When the contact angle is greater than 96°, the droplet does not move. The results show that hydrophilic surfaces promote SDLT on tri-concave fibers. A larger contact area corresponds to larger gradients of the base radius, which leads to a larger driving force *via* eqn (4).

Based on the results above, a novel tri-concave fiber with dual wettability is presented. Two types of wettability are grafted onto the original fiber on the half of the fiber with a contact angle of 45°: dual-HPI (grafted with a contact angle of 10°) and dual-HPO (grafted with a contact angle of 120°), see Fig. 6(c) and (d), respectively. The droplet moves continuously and faster with dual-HPI than on fibers with homogeneous wettability. In contrast, the droplet is stopped by the hydrophobic part of the dual-HPO case. This suggests that the introduction of a more hydrophilic or a more hydrophobic surface wettability can enhance or inhibit SDLT, respectively.

3.6. Discussion

All the living creatures need water. After 3 billion years of evolution, many species have demonstrated effective solutions to ensure their water safety.[24] These solutions usually involve species with unique chemistry and structuring on or within their body that help to dictate the movement of water.[22] The cactus spines need to capture dew and condense ambient moisture to form droplets, and then quickly deliver the droplets to keep alive. Therefore, the spines form the conical shape and microridges to maximize the ability of transporting droplets. In addition to the Mammillaria elongata var. intertexta cactus studied in our previous work,[15] microridges are also observed on other cacti, such as Opuntia microdasys.[14] Interestingly and surprisingly, other spices facing the needs of droplet transport have also formed structures of microridges. The Namib grass Stipagrostis sabulicola relies on grooves within the leaf surface to guide droplets and collect water.[50] Sarracenia trichomes need to condense ambient moisture to form droplets, and quickly transport the droplets to the peristome surface to keep the pitcher mouth wet and slippery.[3] Parallel hierarchical microchannels with rids are observed on trichomes surface. Overall, the microridge is a representative structure that many creatures have evolved to collect water, having great potential in droplets manipulation and microfluidic system.

4. Conclusions

We have found that the concave shape is more suitable for mimicking microridges on cactus spines after studying four types of cross sections. Two modes of droplets motion on a conical fiber are found: annular motion and side motion. A theoretical model is proposed to reveal the mechanism of droplets side motion on concave cross-sections. The results show that microridges can reduce the base radius and the contact area of the droplets, thereby increasing the driving force and reducing the frictional force. This microridge structure inspires a conical fiber with tri-concave cross section. Due to the enlarged Laplace pressure difference and decreased contact area, droplets on such conical fibers spontaneously move at a greater velocity and a longer distance, even with a low surface tension. A tri-concave fiber with dual-wettability is also presented. The introduction of a more hydrophilic or a more hydrophobic surface wettability can enhance or inhibit SDLT. We envision that the present results will open new prospects for droplet manipulation, microfluidics, and fiber system manufacture.

Author contributions

L. Guo and G. H. Tang participated in the design of this study. L. Guo and M. Y. Yang performed the simulation and the theoretical analysis. L. Guo and Z. G. Liu prepared the manuscript. S. Kumar and G. H. Tang carried out the manuscript editing and review. The authors declare no competing financial interest.

Conflicts of interest

There are no conflicts to declare.

Acknowledgements

References

1 B. B. Hu, Z. F. Duan, B. J. Xu, K. J. Zhang, Z. X. Tang, C. Lu, M. J. He, L. Jiang and H. Liu, *J. Am. Chem. Soc.*, 2020, **142**, 6111–6116.

2 J. Li and Z. Guo, *Nanoscale*, 2018, **10**, 13814–13831.

3 H. W. Chen, T. Ran, Y. Gan, J. J. Zhou, Y. Zhang, L. W. Zhang, D. Y. Zhang and L. Jiang, *Nat. Mater.*, 2018, **17**, 935–943.

4 Y. Chen and Y. Zheng, *Nanoscale*, 2014, **6**, 7703–7714.

5 Q. A. Meng, B. J. Xu, M. J. He, R. X. Bian, L. L. Meng, P. W. Wang, L. Jiang and H. Liu, *ACS Appl. Mater. Interfaces*, 2018, **10**, 26819–26824.

6 W. Liu, P. Fan, M. Cai, X. Luo, C. Chen, R. Pan, H. Zhang and M. Zhong, *Nanoscale*, 2019, **11**, 8940–8949.

7 J. Q. Li, X. F. Zhou, J. Li, L. F. Che, J. Yao, G. McHale, M. K. Chaudhury and Z. K. Wang, *Sci. Adv.*, 2017, **3**, eaao3530.

8 H. Kai, R. Toyosato and M. Nishizawa, *RSC Adv.*, 2018, **8**, 15985–15990.

9 K. Li, J. Ju, Z. X. Xue, J. Ma, L. F. Feng, S. Gao and L. Jiang, *Nat. Commun.*, 2013, **4**, 2276.

10 B. Xu, Q. B. Wang, Q. A. Meng, M. J. He, C. Guo, L. Jiang and H. Liu, *Adv. Funct. Mater.*, 2019, **29**, 1900487.

11 K. C. Park, P. Kim, A. Grinthal, N. He, D. Fox, J. C. Weaver and J. Aizenberg, *Nature*, 2016, **531**, 78–82.

12 M. Prakash, D. Quere and J. W. M. Bush, *Science*, 2008, **320**, 931–934.

13 Y. M. Zheng, H. Bai, Z. B. Huang, X. L. Tian, F. Q. Nie, Y. Zhao, J. Zhai and L. Jiang, *Nature*, 2010, **463**, 640–643.

14 J. Ju, H. Bai, Y. M. Zheng, T. Y. Zhao, R. C. Fang and L. Jiang, *Nat. Commun.*, 2012, **3**, 1247.

15 L. Guo and G. H. Tang, *Int. J. Heat Mass Transfer*, 2015, **84**, 198–202.

16 H. W. Chen, P. F. Zhang, L. W. Zhang, H. L. Iu, Y. Jiang, D. Y. Zhang, Z. W. Han and L. Jiang, *Nature*, 2016, **532**, 85–89.

17 Y. Jiao, X. Lv, Y. Zhang, C. Li, J. Li, H. Wu, Y. Xiao, S. Wu, Y. Hu, D. Wu and J. Chu, *Nanoscale*, 2019, **11**, 1370–1378.

18 H. Zhou, X. S. Jing and Z. G. Guo, *Langmuir*, 2020, **36**, 6801–6810.

19 J. Wang, S. Z. Yi, Z. L. Yang, Y. Chen, L. L. Jiang and C. P. Wong, *ACS Appl. Mater. Interfaces*, 2020, **12**, 21080–21087.

20 Q. An, J. S. Wang, F. Zhao and L. Wang, *RSC Adv.*, 2020, **10**, 9318–9323.

21 S. Z. Yi, J. Wang, Z. P. Chen, B. Liu, L. Ren, L. Liang and L. L. Jiang, *Adv. Mater. Technol.*, 2019, **4**, 1900727.

22 D. Gurera and B. Bhushan, *J. Colloid Interface Sci.*, 2019, **551**, 26–38.

23 A. Mahmood, S. Chen, C. L. Chen, D. Weng and J. D. Wang, *J. Phys. Chem. C*, 2018, **122**, 14937–14944.

24 D. Gurera and B. Bhushan, *Philos. Trans. R. Soc., A*, 2018, **377**, 20180269.

25 C. J. Lv, C. Chen, Y. C. Chuang, F. G. Tseng, Y. J. Yin, F. Grey and Q. S. Zheng, *Phys. Rev. Lett.*, 2014, **113**, 026101.

26 M. Y. Cao, J. Ju, K. Li, S. X. Dou, K. Liu and L. Jiang, *Adv. Funct. Mater.*, 2014, **24**, 3235–3240.

27 J. Y. Huang, Y. C. Lo, J. J. Niu, A. Kushima, X. F. Qian, L. Zhong, S. X. Mao and J. Li, *Nat. Nanotechnol.*, 2013, **8**, 277–281.

28 C. Duprat, S. Protiere, A. Y. Beebe and H. A. Stone, *Nature*, 2012, **482**, 510–513.

29 E. Lorenceau and D. Quere, *J. Fluid Mech.*, 2004, **510**, 29–45.

30 X. J. Li, Y. Yang, L. Y. Liu, Y. Y. Chen, M. Chu, H. F. Sun, W. T. Shan and Y. Chen, *Adv. Mater. Interfaces*, 2019, **7**, 1901752.

31 H. Y. Bai, T. H. Zhao, X. S. Wang, Y. C. Wu, K. Li, C. M. Yu, L. Jiang and M. Y. Cao, *J. Mater. Chem. A*, 2020, **8**, 13452–13458.

32 Y. Chen, K. Li, S. Zhang, L. Qin, S. Deng, L. Ge, L. P. Xu, L. Ma, S. Wang and X. Zhang, *ACS Nano*, 2020, **14**, 4654–4661.

33 E. Papadopoulou, C. M. Megaridis, J. H. Walther and P. Koumoutsakos, *ACS Nano*, 2019, **13**, 5465–5472.

34 Y. Zheng, J. Cheng, C. Zhou, H. Xing, X. Wen, P. Pi and S. Xu, *Langmuir*, 2017, **33**, 4172–4177.

35 Y. Y. Song, Y. Liu, H. B. Jiang, S. Y. Li, C. Kaya, T. Stegmaier, Z. W. Han and L. Q. Ren, *Nanoscale*, 2018, **10**, 3813–3822.

36 S. Huang, J. Li, L. Liu, L. Zhou and X. Tian, *Adv. Mater.*, 2019, 1901417.

37 S. Dhiman, K. S. Jayaprakash, R. Iqbal and A. K. Sen, *Langmuir*, 2018, **34**, 12359–12368.

38 J. Li, X. L. Tian, A. P. Perros, S. Franssila and V. Jokinen, *Adv. Mater. Interfaces*, 2014, **1**, 1400001.

39 M. Soltani and K. Golovin, *Adv. Funct. Mater.*, 2021, 2107465.

40 L. Zhang, Z. Q. Guo, J. Sarma, W. W. Zhao and X. M. Dai, *Adv. Funct. Mater.*, 2021, **31**, 2008614.

41 D. Niu and G. H. Tang, *RSC Adv.*, 2018, **8**, 24517–24524.

42 L. Guo, G. H. Tang and S. Kumar, *Langmuir*, 2019, **35**, 16377–16387.

43 S. Gao, Q. Liao, W. Liu and Z. Liu, *J. Phys. Chem. Lett.*, 2018, **9**, 13–18.

44 Z. Li, G. H. Hu, Z. L. Wang, Y. B. Ma and Z. W. Zhou, *Phys. Fluids*, 2013, **25**, 072103.

45 M. Arienti, W. Pan, X. Li and G. Karniadakis, *J. Chem. Phys.*, 2011, **134**, 204114.

46 S. Aphinyan, E. Y. M. Ang, J. J. Yeo, T. Y. Ng, R. M. Lin, Z. S. Liu and K. R. Geethalakshmi, *Modell. Simul. Mater. Sci. Eng.*, 2019, **27**, 055005.

47 J. L. Jones, M. Lal, J. N. Ruddock and N. A. Spenley, *Faraday Discuss.*, 1999, **112**, 129–142.

48 C. Cupelli, B. Henrich, T. Glatzel, R. Zengerle, M. Moseler and M. Santer, *New J. Phys.*, 2008, **10**, 043009.

49 R. D. Groot and P. B. Warren, *J. Chem. Phys.*, 1997, **107**, 4423–4435.

50 A. Roth-Nebelsick, M. Ebner, T. Miranda, V. Gottschalk, D. Voigt, S. Gorb, T. Stegmaier, J. Sarsour, M. Linke and W. Konrad, *J. R. Soc., Interface*, 2012, **9**, 1965–1974.